High Performance Polymers

http://hip.sagepub.com

POSS-Polyimide Nanocomposite Films: Simulated Hypervelocity Space Debris and Atomic Oxygen Effects

R. Verker, E. Grossman, I. Gouzman and N. Eliaz

High Performance Polymers 2008; 20; 475
DOI: 10.1177/0954008308089710

The online version of this article can be found at:
http://hip.sagepub.com/cgi/content/abstract/20/4-5/475

Published by:
SAGE
http://www.sagepublications.com

POSS-Polyimide Nanocomposite Films: Simulated Hypervelocity Space Debris and Atomic Oxygen Effects

R. VERKER[1]
E. GROSSMAN
I. GOUZMAN
Space Environment Group, Soreq NRC, Yavne 81800, Israel

N. ELIAZ
School of Mechanical Engineering, Tel-Aviv University, Ramat Aviv, Tel-Aviv 69978, Israel

(Received 20 December 2006; accepted 3 January 2008)

Abstract: The combined effect of hypervelocity space debris impact and atomic oxygen (AO) attack on the degradation of reinforced polyhedral oligomeric silsesquioxanes (POSS)-polyimide films was studied. A laser-driven flyer (LDF) system was used to accelerate aluminum flyers to impact velocities of up to 3 km s^{-1}. The impacted films were exposed to an RF-plasma source, which was used to simulate the effect of AO in the low Earth orbit. Scanning electron microscopy (SEM) was used to characterize the fracture morphology. The extent of damage in POSS-polyimide impacted films was found to be much smaller compared to POSS-free films, insinuating on a toughening mechanism developed due to POSS incorporation. When exposed to air RF-plasma, the impacted POSS-free film revealed a synergistic effect associated with a large increase in the erosion rate while impacted POSS-containing samples showed improved erosion resistance. The increased erosion rate of the impacted POSS-free film is explained by formation of residual stresses that affect the oxidation mainly by increasing the diffusivity of oxygen.

Keywords: POSS, polyimide, atomic oxygen, space debris

1. INTRODUCTION

Most satellites today are being launched into low Earth orbit (LEO) altitudes, from 200 to 1000 km. Natural or man-made LEO space environment possesses many obstacles to a successful spacecraft mission. The degrading environment for polymers includes atomic oxygen (AO), ultraviolet (UV) radiation, ionizing radiation, ultrahigh vacuum (UHV), thermal cycles, micrometeoroids and orbital debris. Due to separate, combined or syner-

High Performance Polymers, **20:** 475–491, 2008 DOI:10.1177/0954008308089710

Figure 1 appears in color online: http://hip.sagepub.com

gistic interactions with these space hazards, polymers in particular suffer a relatively rapid erosion, structure modification and surface roughening. This might lead to irreversible degradation of optical, thermal, electrical and mechanical properties [1,2].

Micrometeoroids originate naturally from planetary or asteroidal collisions and cometary ejecta [3]. Hypervelocity debris at LEO altitudes are man-made constituents, originating from large objects such as spent satellites and rockets, consisting mostly of small objects such as aluminum oxide fuel particles, paint chips and fragmentation objects from collisions of these bodies in orbit [3,4]. Typical velocities of debris particles range from a few kilometers per second up to 16 km s^{-1}, making these hypervelocity particles a threat to spacecraft [5,6]. Debris traveling at ultrahigh velocities generates temperatures of approximately 4700°C and pressures of several megabar upon colliding with a surface [7].

Accumulation of impacts over the large surface area of solar panels has led, in some cases, to degradation in efficiency [8]. In the case of composites, if a complete penetration occurs, it can lead to further breakdown of the composite during subsequent exposure to AO or vacuum UV (VUV). Debris impacts into polymer films occur quite often since they are used extensively onboard spacecraft, mainly as thermal blankets [6]. Thermal control materials on the Long Duration Exposure Facility (LDEF) have demonstrated significant synergistic effects of orbital debris with other space environmental hazards. These synergistic effects further expand the damaged area caused by direct impacts. For example, the top surface of a metalized Mylar sample aboard the LDEF was completely eroded, exposing the interior surfaces to VUV radiation, AO and thermal cycling [6].

Kapton surfaces coated with SiO_2 have been shown to exhibit AO erosion yields less than one percent of the erosion yield of unprotected Kapton. Although the SiO_2 coating itself is resistant to AO, inherent and hypervelocity debris-induced defects in the coating will permit AO attack of the underlying polymer and undercut the coating [9].

A promising approach toward the production of LEO survivable polymers is to incorporate Polyhedral Oligomeric Silsesquioxanes (POSS) into the polymeric chains [10–13]. Previous work showed that POSS-containing polyimides have significantly lower erosion yields than Kapton, since AO irradiation results in formation of SiO_2 passivation layer which protects the underlying polymer from further AO attack [10]. It was also shown that POSS-polyimides gained weight during AO exposure and healed microcracks that were present [11]. However, the effect of AO erosion on POSS-polyimide surfaces already impacted by hypervelocity debris has not yet been studied.

In this work, the effect of hypervelocity impacts combined with ground simulated AO exposure on the fracture of nano-reinforced POSS-polyimide films was studied. Tri-SilanolPhenyl-POSS was incorporated into the polyimide network by weak cross-linking, forming an interpenetrating network, making the POSS-polyimide blend oxidation-resistant [14,15].

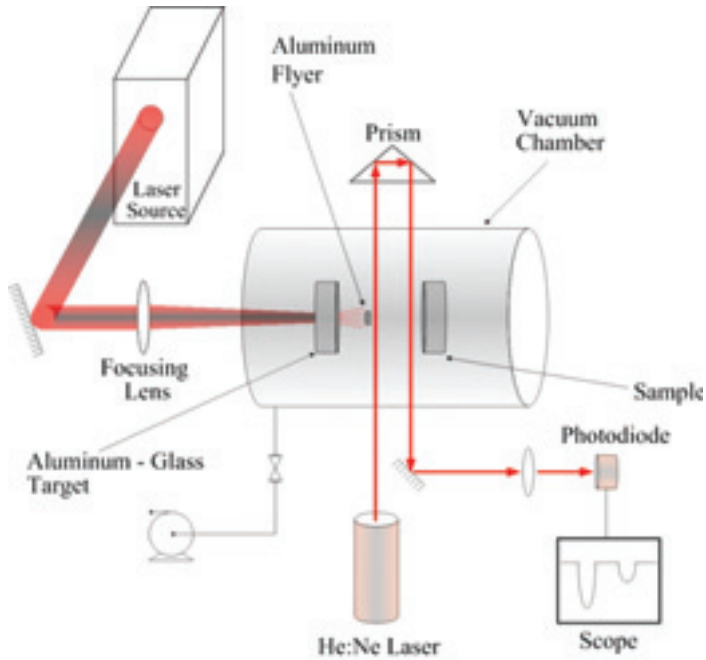

Figure 1. Schematic diagram of the experimental set-up.

2. EXPERIMENTAL

2.1. The laser-driven flyer method

The laser-driven flyer (LDF) method was used to generate simulated space hypervelocity debris with dimensions ranging from ten to hundreds of microns and velocities of up to 3 km s^{-1}. LDF is an attractive technique for debris simulation due to its relative simplicity, low cost, ease of incorporation into a vacuum facility and high shot-rate capability [7,16,17].

Figure 1 shows a schematic drawing of the LDF system. The system consists of a high-power Titanium:Sapphire laser (Thales Laser) with a variable pulse length of 50 fs to 300 ps, the latter being used in this work. The wavelength in which the laser operates is 810 nm, and the range of pulse energies available is 250–750 mJ. The laser beam is guided through a set of mirrors into a vacuum chamber operating at a base pressure of 65 mTorr. Before entering the chamber, the beam passes through a focusing lens attached to a linear motion mechanism. Inside the chamber, the laser beam irradiates a 12 μm thick pure aluminum foil through a BK7 glass substrate. The aluminum foil was bonded to the BK7 glass using a field-assisted diffusion bonding process [17] (this laminate being referred to, hereafter, as target). The beam passes through the glass without interacting

with it, until it hits the aluminum/glass interface. At the interface, a high-temperature and high-pressure plasma is formed, which then expands perpendicularly to the foil.

The theory of plasma expansion, which is responsible for the production of the ultrahigh-velocity flyers, is described in detail elsewhere [18]. Briefly, the expanding plasma induces a shock wave in the target, moving faster than the speed of sound toward the free (rear) surface. When the shock wave reaches the free surface, the latter is accelerated and the former is reflected as a rarefaction wave. The rarefaction wave, moving in an opposite direction, causes deceleration of the free surface. The two rarefaction waves (i.e. the tail of the initial pressure wave and the wave reflected from the free surface), running in opposite directions, generate tension in the material. When the tension (i.e. negative pressure) exceeds the material spall strength, a spall forms in a plane parallel to the rear surface. A pressure gradient between the plasma high pressure on one side of the spall and the vacuum low pressure on the other side of the spall causes the spalled layer acceleration, resulting in an aluminum layer 1 mm in diameter flying away at the ultrahigh velocity of up to about 3 km s^{-1}. The accelerated aluminum layer is composed of small flyers, the largest being of the order of 30–50 μm in size, moving at about the same ultrahigh velocity. The smaller flyers, which are on the nanometer scale, are slower and exhibit a much wider velocity distribution. The aluminum flyers are accelerated towards a polymer sample placed at a distance 12 mm from the target.

2.2. Flyer velocity measurements

The flyer velocity is a function of the laser beam spot size and pulse energy. Figure 1 also shows the set-up used to measure the flyer velocity *in situ*. A continuous He:Ne laser beam is set orthogonal to the flyer's trajectory and, using a prism, the beam crosses the flyer's path twice. The two parallel beams were set at a distance of 13 mm from each other. A photodiode attached to an oscilloscope receives the continuous laser signal. As the flyer crosses and blocks the continuous laser path, velocity can be calculated from the two peaks detected by the oscilloscope.

2.3. RF plasma AO ground simulation system

A conventional RF plasma reactor (15 W, 13.56 MHz, Model PDC-3XG from Harrick), operating at 500 mTorr of air, was used to simulate the effect of AO in the low Earth orbit [19]. Samples were positioned on a specially designed sample holder, which allows simultaneous exposure of up to six different samples. The samples were positioned 100 mm downstream from the reactor in the afterglow region, where they were exposed to a mixture of atomic and molecular oxygen, excited species and VUV radiation. Nevertheless, the contribution of ions, VUV and excited species is reduced compared to the RF plasma reactor environment [20]. Although LEO AO is hyperthermal, the RF plasma environment with thermal AO is considered to be a useful tool for materials evaluation. The space equivalent AO flux at the sample position was 4×10^{14} O-atoms cm^{-2} s^{-1}. Atomic oxygen equivalent fluence measurements were conducted based on 25 μm thick

Kapton-HN film (DuPont, Inc.) mass loss, assuming an erosion yield of 3×10^{-24} cm^3 per O-atoms [21]. The erosion yield was determined gravimetrically, using an analytical balance (Model UM3 from Mettler) with an accuracy of ± 1 μg.

2.4. Materials and characterization techniques

The materials studied in this work were blends of oxydianiline – pyromellitic dianhydryde (ODA-PMDA) polyimide (Pyre-M.L. RC-5019 by Industrial Summit Technology, Co.) and TriSilanolPhenyl-POSS (Hybrid Plastics, Inc.). Samples were produced in the form of thin films (25–30 μm thick), with different POSS contents of 0, 5, 10 and 15 wt %. POSS-polyimide films were produced at a bench-scale process by casting and curing a pre-mixed solution of polyamic acid and POSS in N-methyl-Pyrrolidone solvent [22]. The curing of the pre-mixed solution is based on a process developed by DuPont, Inc. After casting the pre-mixed solution on a Si wafer, the samples were heated to 200°C in moist air at a ramp rate of 4°C min^{-1} and held for a period of 30 min. In a second temperature cycle, the samples were heated to 350°C in the presence of pure nitrogen at a ramp rate of 2°C min^{-1} and held for a period of 60 min. In order to avoid residual stresses, the final stage was slow cooling at a rate of 2°C min^{-1} down to room temperature [23]. At room temperature, the POSS-polyimide films were peeled-off the Si wafer. In addition, a commercial 25 μm thick Kapton-HN film (DuPont, Inc.) was studied. Kapton-HN is also used in this work as a reference material for the 0 wt % POSS-polyimide and for evaluating the AO equivalent fluence.

The morphology of fractured surfaces resulting from the debris impacts at ultrahigh velocities was studied using an Environmental SEM (ESEM, model Quanta 200 from FEI). This microscope allows characterization of non-conductive samples without the need for a conductive coating.

XPS spectra were obtained using non-monochromatized Al Kα radiation (1486.6 eV) and a hemispherical CLAM 2 (VG Microtech) analyzer. The binding energy scale was calibrated with the use of an Ag($3d_{5/2}$) line at 368.3 eV as a reference.

3. RESULTS AND DISCUSSION

3.1. RF-plasma erosion tests

In order to understand the contribution of the TriSilanolPhenyl-POSS to the oxidation resistance of the polyimide, an RF-plasma erosion test was performed. The four different POSS-containing samples and a Kapton-HN sample were exposed simultaneously to the plasma afterglow, the exposed area being 0.5 cm^2 per sample. The erosion yield was determined gravimetrically by weighing the samples on an analytical balance (Model UM3 from Mettler). The samples were weighted periodically, and the AO equivalent fluence was determined using the Kapton-HN reference sample. The erosions of the POSS-polyimide and Kapton-HN samples are plotted in figure 2 as a function of the AO

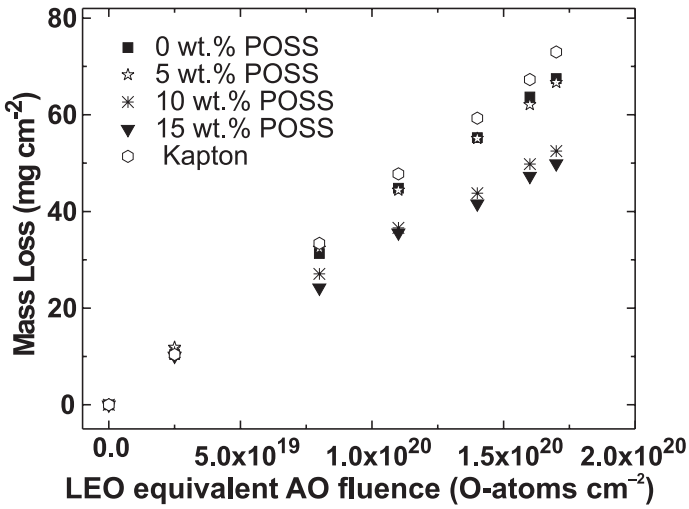

Figure 2. Mass loss measurements for 0, 5, 10 and 15 wt.% POSS-polyimide and for Kapton-HN samples.

equivalent fluence. The erosion of all five samples appeared to increase linearly with the fluence. According to these measurements, the higher the POSS content of a sample, the smaller the erosion rate.

The 0 and 5 wt.% POSS-polyimide samples reveal similar erosion rates and low AO erosion resistance. Better AO erosion resistance is observed when the POSS content is increased to 10 and 15 wt.%. The 15 wt.% POSS-polyimide sample reached an erosion rate of 68% of the erosion rate of Kapton-HN. It appears that 5 wt.% is not sufficient to generate any significant erosion resistance towards AO attack. On the other hand, the 10 wt.% POSS generates almost the same erosion resistance as that produced by the 15 wt.% POSS-containing sample.

3.2. Ultrahigh-velocity impacts on POSS-polyimide films

The effect of POSS content on the extent of damage of impacted samples is demonstrated in figure 3. The fractures were created using flyer velocities of 1.8–2.8 km s^{-1}. All ESEM images were taken from the flyer exit side.

To evaluate and compare the impact damage, one should consider the film thickness and the flyer impact velocity. The effect of film thickness and flyer velocity on the amount of damage to Kapton-HN films (i.e. 0 wt.% POSS) due to ultrahigh-velocity impacts was discussed in detail elsewhere [24]. In general, as the film becomes thicker, its ability to absorb energy and slow the flyers increases. Consequently, the strain rate associated with the impact process is reduced, and the fractured surface tends to shift from brittle to

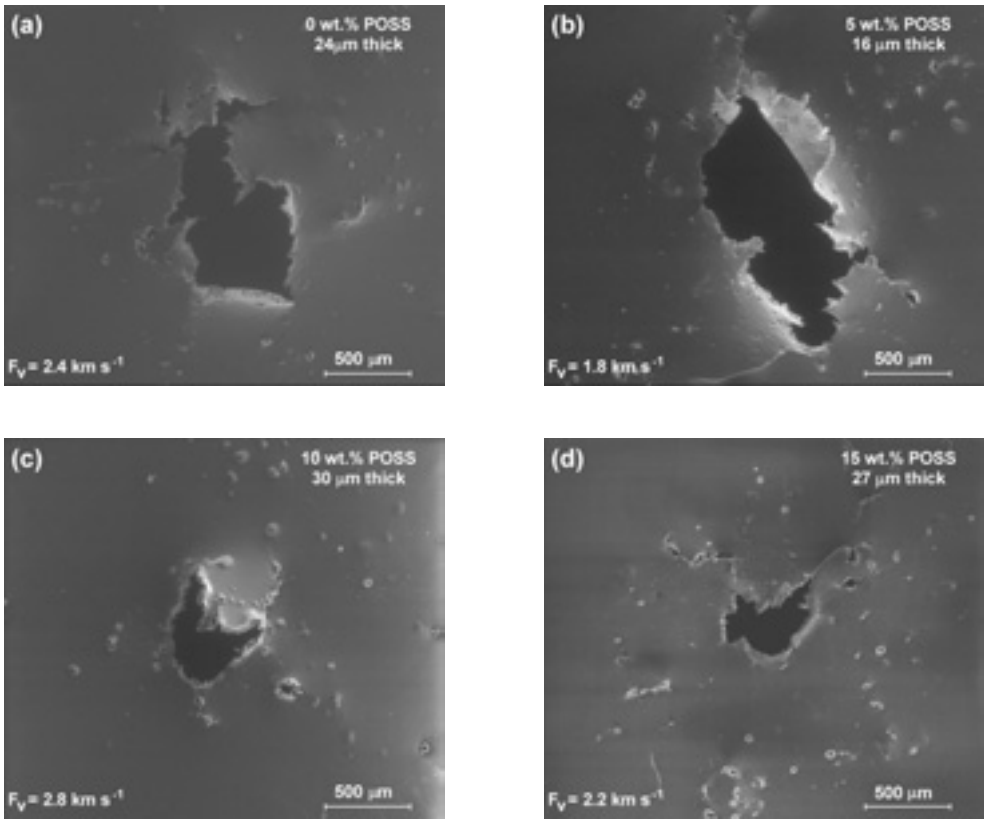

Figure 3. ESEM images of (a) 0 wt.%; (b) 5 wt.%; (c) 10 wt.% and (d) 15 wt.% 16–30 μm thick POSS-polyimide films, impacted by flyers at velocities of 1.8–2.8 km s^{-1}.

ductile. The impact on Kapton-HN films introduces high temperatures ($T > T_g$) at the central impact region, and lower temperatures ($T < T_g$) at remote regions. Consequently, the central impact region is characterized by ductile-like fractures, whereas the remote radial crack regions are characterized by a brittle-like fracture. Considering the above variables, a comparison of the ultrahigh-velocity impacts on the 0 wt.% POSS film to that on 10 and 15 wt.% POSS films reveals that adding POSS to the polyimide reduces the extent of damage created by the impact. The perforated area of the 10 and 15 wt.% samples, due to shearing and bending of the film, is about third of the perforated area of the 0 wt.% sample. Addition of POSS contributes significantly to the polyimide film hardness, as demonstrated by residual impression nanoindentation measurements [25]. The addition of POSS also improves other mechanical properties such as Young's modulus and tensile strength [22]. It appears that POSS-containing films exhibit better ultrahigh-velocity impact toughness compared to the 0% POSS-containing film. The ability of

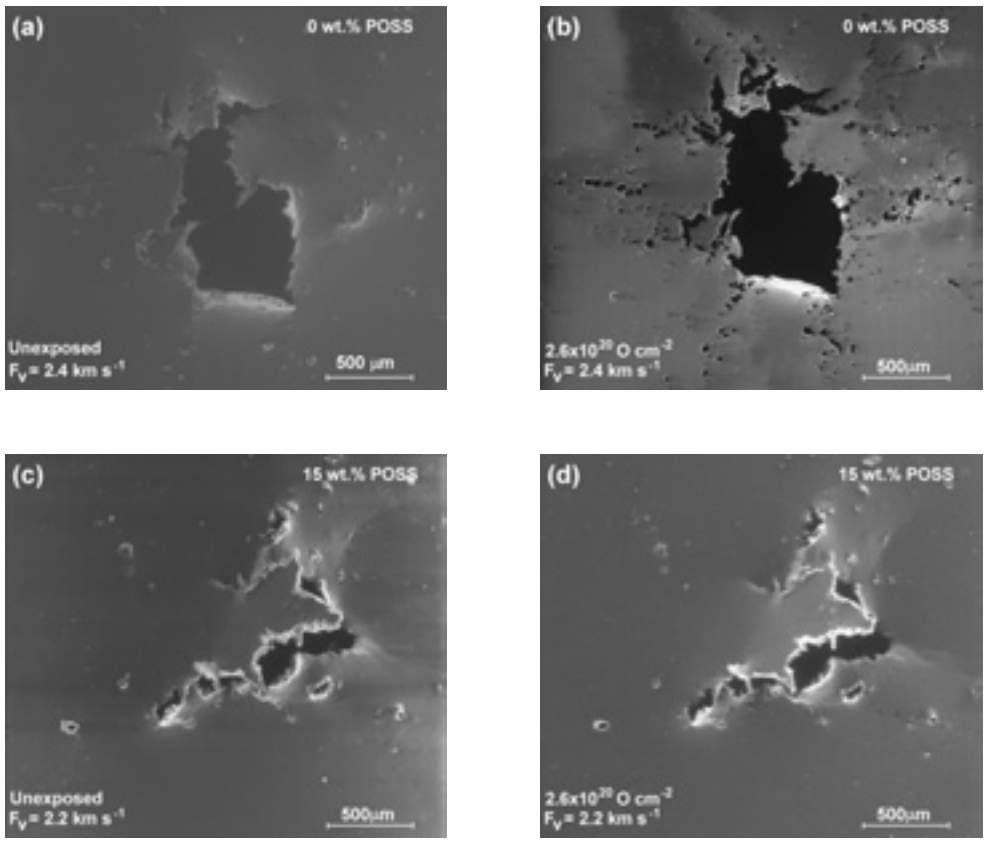

Figure 4. ESEM images of 0 and 15 wt.% POSS-polyimide films impacted by flyers at velocities of (a) 2.4 and (c) 2.2 km s^{-1}, subsequently exposed to AO equivalent fluence of 2.6×10^{20} O-atom cm^{-2} (images (b) and (d), respectively).

POSS to improve the ultrahigh-velocity impact toughness of polyimide films is discussed further below.

3.3. Synergistic effect of ultrahigh-velocity impacts and RF-plasma exposure

Figure 4 demonstrates the synergistic effect of ultrahigh-velocity impacts and RF-plasma erosion on 0 and 15 wt.% POSS samples. The fractures of the 0 wt.% POSS samples were created using flyers with a velocity of 2.4 km s^{-1}. Similarly, the fractures of the 15 wt.% POSS samples were created using flyers with a velocity of 2.2 km s^{-1}.

After being impacted by the ultrahigh-velocity flyers, the samples were exposed to AO equivalent fluence of 2.6×10^{20} O-atom cm^{-2}. All ESEM images were taken from the

Table 1. Perforated area values of the 0 and 15 wt.% POSS samples prior to and after AO erosion.

AO equivalent fluence	A_p (mm^2)	
(O-atom cm^{-2})	0 wt.% POSS	15 wt.% POSS
Unexposed	0.47	0.09
2.6×10^{20}	0.70	0.11

flyer exit side. Significant erosion of the 0 wt.% POSS-containing films is evident after the exposure to AO equivalent fluence of 2.6×10^{20} O-atom cm^{-2}. The 15 wt.% POSS-containing film, on the other hand, shows better AO erosion resistance. No expansion of existing holes or formation of new holes was observed for the 15 wt.% POSS-polyimide sample after the RF-plasma exposure. Quantification of the amount of erosion on each of the two samples was carried out using the image processing tool of the analySIS software. The perforated area A_p in each of the four images in figure 4 was chosen for comparison of the synergistic effect of ultrahigh-velocity impact and AO erosion on each of the two samples. Each of the four images was transformed to a binary image according to a chosen threshold, which gave the best separation between perforated (white) and non-perforated (black) areas. The results of A_p measurements are summarized in table 1.

According to the results shown in table 1, A_p of the 0 wt.% POSS sample increased from 0.47 for the unexposed sample to 0.70 mm^2 after AO exposure. In comparison, A_p of the 15 wt.% POSS sample increased from 0.09 for the unexposed sample to 0.11 mm^2 after exposure. In terms of A_p, these results reflect a difference of about one order of magnitude in erosion rates of the two samples. For comparison, non-impacted 15 wt.% POSS sample reached an erosion rate of 74% of the erosion rate of 0 wt.% POSS-containing sample, according to gravimetric measurements. The large difference in erosion rate is attributed to the impact-induced residual tensile stress, as discussed below.

A previous study [10] of POSS-dianiline polyimide attributed AO erosion resistance to the formation of SiO_2 passivation layer, which prevents further oxidation of the polymer's carbon backbone. Although TriSilanolPhenyl-POSS polyimide has a different structure, the same mechanism of creating a SiO_2 passivation layer is applicable. Figure 5 shows an XPS spectra of 15 wt.% POSS-polyimide (a) before and (b) after exposure to AO equivalent fluence of 2.6×10^{20} O-atom cm^{-2}. The elemental composition of the 15 wt.% POSS polyimide samples was determined by XPS survey spectra obtained before and after exposure to the AO equivalent fluence. The surface elemental composition (at.%) is summarized in table 2. The carbon atomic concentration decreased drastically after exposure, while the oxygen atomic concentration essentially tripled. The data indicate that the AO irradiation modified the surface mainly to silicon oxide with residues of hydrocarbons. High-resolution XPS spectra (not shown) reveal a chemical shift of 1 eV in the Si 2p peak after AO exposure. This binding energy shift indicates oxidation of the silicon into a passivation layer in the form of SiO_2.

Figure 6 shows higher-magnification ESEM images of the 0 wt.% POSS-polyimide sample (a) unexposed and (b) exposed to AO equivalent fluence of 1.1×10^{20} and (c)

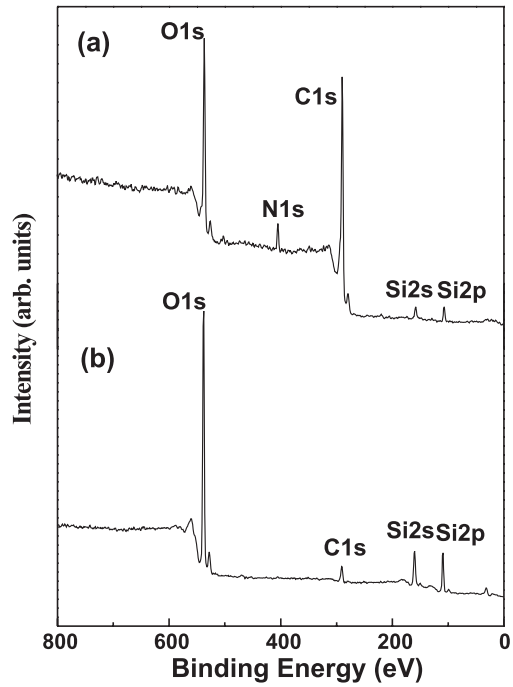

Figure 5. XPS survey spectra of 15 wt.% POSS-polyimide films (a) before and (b) after exposure to AO equivalent fluence of 2.6×10^{20} O-atom cm^{-2}.

Table 2. Elemental composition (at.%) determined from XPS data for 15 wt.% POSS-polyimide samples prior to and after exposure to AO.

	Unexposed	Exposed to AO
O 1s	21.5	61.5
C 1s	72.3	11.0
Si 2p	1.7	27.0
N 1s	4.5	0.5

2.6×10^{20} O-atom cm^{-2}. One can observe the formation of new holes, which are the characteristic outcome feature of the accelerated erosion rate of the 0 wt.% POSS-polyimide sample. After ultrahigh-velocity impact, the 0 wt.% POSS-polyimide film can be characterized by through-holes, as evident on the image upper part, and by some dents (that may be the result of residual stresses within the polymer) along the lower edge of the crack (figure 6a). After exposure of the sample to an AO equivalent fluence of 1.1×10^{20} O-atom cm^{-2}, three main effects are evident (figure 6b): (i) expansion of existing through-holes; (ii) development of new holes at the dented sites; and (iii) formation of a rough

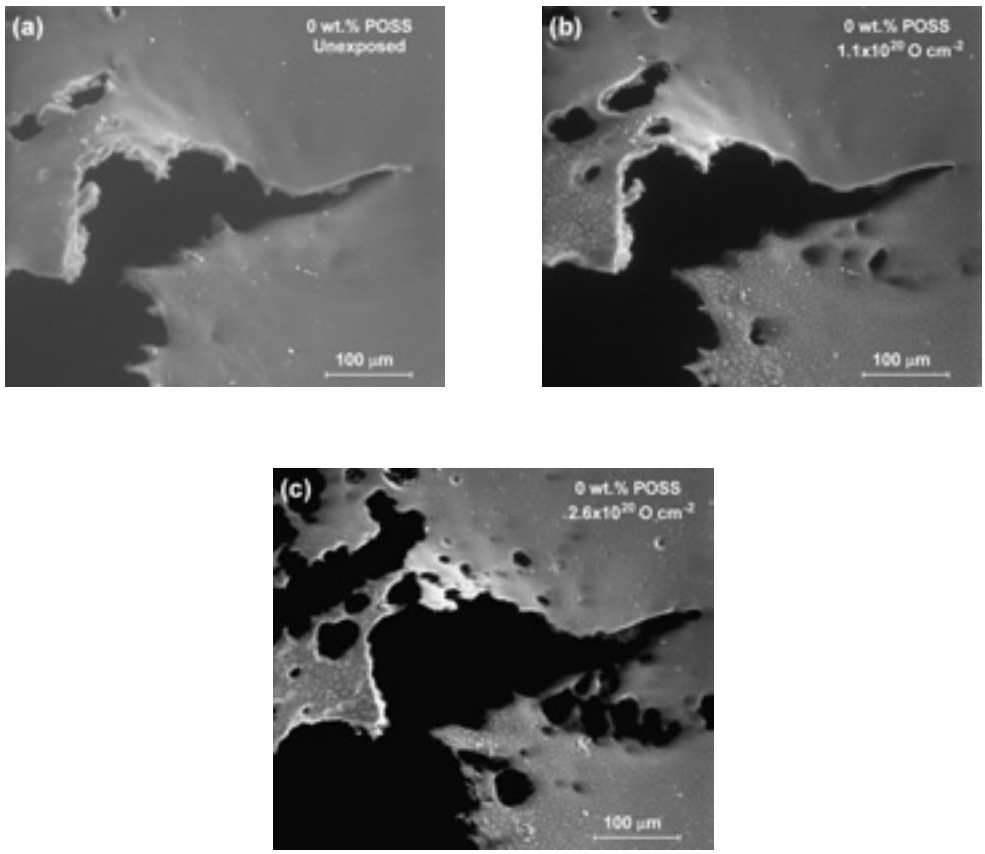

Figure 6. Zoom-in ESEM images of the 0 wt.% POSS-polyimide film impacted by flyers (a) at a velocity of 2.4 km s^{-1} and (b) subsequently exposed to AO equivalent fluence of 1.1×10^{20} and (c) 2.6×10^{20} O-atom cm^{-2}.

surface (at the image left-hand side). On the other hand, the surface on the upper right-hand side appears undamaged, as in the unexposed state.

Further exposure of the sample to an equivalent fluence of 2.6×10^{20} O-atom cm^{-2} resulted in formation of a larger number of new holes, while older holes coalesce (figure 6c). Also evident on figure 6c is that the region mostly susceptible to erosion is the area next to the center of the impact hole where the film is bent, and not near the crack.

A model is proposed to explain the extensive erosion and formation of new macro-holes in the impacted 0 wt.% POSS-containing film due to UV and AO exposure in the RF-plasma afterglow. The new macro-holes formation is a result of a multi-step process [26].

(i) The establishment of a field of residual tensile stresses within the polymer due to the ultrahigh-velocity impacts, and temporary local increase in the average temperature to values that may exceed the glass transition temperature [24].

(ii) An increase in the polymer's local free volume (i.e. the volume that is not occupied by the polymer chains), in regions of higher residual tensile stresses and/or a higher average temperature [27].

(iii) Increased molecular and atomic oxygen diffusion into the polymer due to residual tensile stresses, which reduce the local chemical potential. It is well known that diffusion processes can be motivated by gradients of stress, temperature and/or electrical potential. A hydrostatic tensile stress decreases the chemical potential of an interstitial solute. This is true whether the stress is externally applied or is residual. Since the gradient of chemical potential is the fundamental driving force for diffusion, the flux of solute is defined as

$$J = -\frac{Bc}{N_A}\frac{\partial \mu}{\partial c}\nabla c = -D\nabla c + \frac{DcV_{\text{sol}}}{kT}\nabla\left(\sigma_{\text{h}}\right) \tag{1}$$

where B is the mechanical mobility, c concentration, μ chemical potential, D diffusion coefficient, V_{sol} atomic volume of the solute atom in the material, k Boltzmann constant, N_A Avogadros numbes, T temperature, and σ_h hydrostatic component of the elastic stress field [28–30]. The situation is even more complex in the case of the POSS-polyimide samples studied here. Not only does the ultrahigh-velocity impact establish a field of residual tensile stresses, the local free volume is also increased (for the amorphous phase, as long as the stress is not high enough to induce ordering of the polymer chains and crystallization). It is agreed that the polymer fractional free volume has a major effect on the diffusivity and permeability of molecular oxygen and AO [27]. Furthermore, oxygen diffusion, which is the rate-limiting step in many photo-oxidative reactions [31, 32], can be affected by other factors such as polymer crystallinity, cross-linking and morphology. The latter is a parameter that has an important influence on the rate of polymer photochemical degradation. Micro-cracks, initially developed on the surface at stressed regions, facilitate the diffusion of oxygen into the bulk [31].

(iv) A local increase in the AO-induced erosion rate. In general, AO reaction with polymers is a thermally activated, two-step process. In the first step, AO and molecular oxygen diffuse into the polymer. In the present study, VUV radiation from the RF plasma interacts with the diffused molecular oxygen to form AO. In the second step, the AO, either diffused oxygen atoms or VUV dissociated oxygen molecules, react more readily with reactive sites. The formation of reactive sites in the underneath layers of the polymer are a result of VUV radiation, which initiates a destruction of the aromatic polyimide groups [33–35]. The reaction's volatile products (i.e. H_2O, CO and CO_2) then diffuse towards the film surface and desorb. One of the effects of the stress is to decrease the efficiency of recombination of photochemically gen-

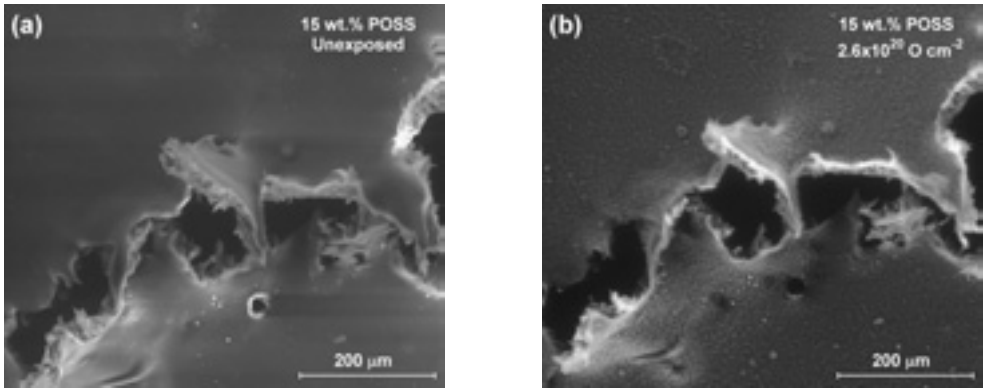

Figure 7. Zoom-in ESEM images of the 15 wt.% POSS-polyimide film impacted by flyers at (a) a velocity of 2.2 km s^{-1} and (b) subsequently exposed to AO equivalent fluence of 2.6×10^{20} O-atom cm^{-2}.

erated radical pairs, by increasing the separation between them. Consequently, the probability of radical trapping and radical-dependent reactions is increased. This leads to an increased rate of degradation, which first takes place on the polymer's surface thus affecting its morphology, followed by bulk etching [31].

(v) The formation of new macro-holes, which replicate the distribution of residual tensile stresses.

It is believed that different regions in the 0 wt.% POSS-polyimide sample were sustained to different amounts of residual tensile stresses.

The expansion of existing through-holes (figure 6b) due to AO erosion is obvious. The development of new holes at the dented sites is attributed to two facts. (i) The dented sites are thinner compared to other regions in the film. This alone can promote the formation of new through-holes because a smaller amount of AO equivalent fluence is required for perforation. (ii) The formation of these dented sites is attributed to residual tensile stresses, which make them susceptible to AO erosion (as previously discussed). The formation of a rough surface at the image left-hand side is also attributed to residual tensile stresses at this region, which promoted faster degradation reactions, affecting its morphology and making it rougher. Increase in AO equivalent fluence (figure 6c) leads to the formation of new holes via the mechanisms mentioned above, as well as expansion of older holes until they coalesce.

Figure 7 shows ESEM images of impacted 15 wt.% POSS-polyimide sample (a) unexposed and (b) exposed to 2.6×10^{20} O-atom cm^{-2} AO equivalent fluence. The exposure to the RF-plasma environment resulted in erosion of the 15 wt.% POSS-polyimide film surface and made it rougher. The roughness is equivalent all over the film surface, suggesting that no residual stress exists beneath the surface.

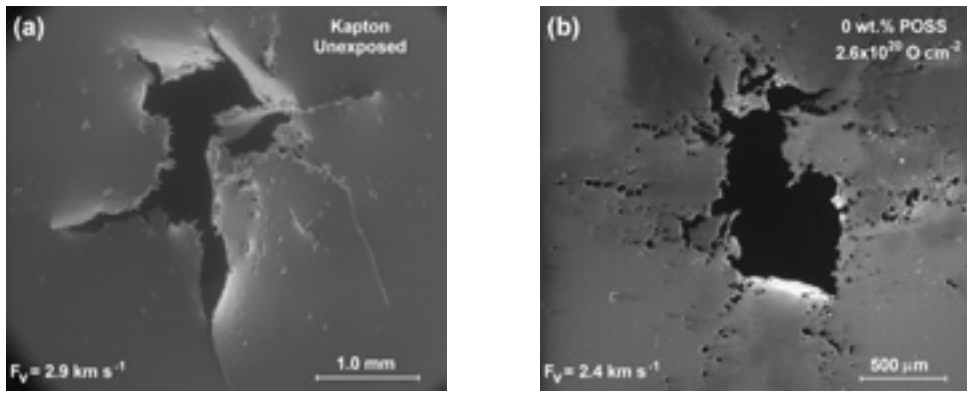

Figure 8. ESEM images of 25 μm thick Kapton-HN film, impacted by 2.9 km s^{-1} flyers. (a) Radial cracking that forms a star-like pattern is evident. (b) 0 wt.% POSS sample impacted by 2.4 km s^{-1} flyers and subsequently exposed to 2.6×10^{20} O-atom cm^{-2} AO equivalent fluence. New holes were formed, also in a radial star-like pattern.

The unexposed fractured surface morphology (fractography), which is of ductile type (figure 7a), can be characterized as porous with elongated thin features emanating from the fractured surfaces. A fluence of 2.6×10^{20} O-atom cm^{-2} (figure 7b) eroded most of the elongated thin features and around the through-hole (located at the image lower part). This is attributed to the roughness of the fracture surface, which facilitates diffusion of AO into the bulk, thus resulting in a higher local erosion rate. Nevertheless, even in the high-magnification ESEM images, no formation of new holes is evident for the 15 wt.% POSS-polyimide sample. Since the model suggests that new holes are most likely to be formed in sites where residual tensile stresses exist, it appears – considering this parameter and the roughness issue mentioned above – that no residual stresses were introduced in the case of 15 wt.% POSS-polyimide sample.

Further support for the model, which explains new holes formation by AO erosion in residual tensile stressed regions, is shown in figure 8. Figure 8a shows a 25 μm thick Kapton-HN film, impacted by a 2.9 km s^{-1} flyer [24]. The impacted Kapton-HN is characterized by radial cracking around a central impact zone, forming a star-like pattern. Figure 8b shows the 2.4 km s^{-1} impacted 0 wt.% POSS-polyimide sample after exposure to 2.6×10^{20} O-atom cm^{-2} AO equivalent fluence. Erosion is most apparent from the expansion of holes formed by the ultrahigh-velocity impact and formation of a large number of new holes. These new holes tend to be formed in a radial star-like pattern around the sample's central impact zone. The kinetic energy that the Kapton-HN sample experienced was high enough for long radial cracks to develop, as a secondary process, after pieces of Kapton-HN were sheared-off from the central impact zone. On the other hand, the kinetic energy that the 0 wt.% POSS-polyimide sample experienced was not as high, hence shorter cracks were formed. However, the formation of the new holes (along with holes

created directly by the ultrahigh-velocity impacts) in a radial star-like pattern around the sample's central impact zone supports the residual tensile stress model. It appears that a residual tensile stress field developed within the polymer film in radial directions, as is the case of the Kapton-HN sample (figure 8a). When exposed to AO equivalent fluence these residual stresses, which already caused a local increase in the polymer free volume, initiated the process of local high-rate degradation. This has been facilitated by diffusion of oxygen into the bulk of the polymer, leading to the formation of the star-like pattern. Under further RF-plasma erosion, these holes grew and, eventually, coalesced as shown in figure 6c.

4. CONCLUSIONS

Ultrahigh-velocity impact and simulated AO exposure effects on POSS-polyimide films were studied. Addition of 15 wt.% POSS to the polyimide increased the AO erosion durability due to formation of SiO_2 passivation layer. The results of ultrahigh-velocity impacts into the POSS-polyimide films insinuate on improved ultrahigh-velocity impact toughness of POSS-containing films, compared to pure polyimide films. A synergistic erosion effect was observed under AO exposure of the previously hypervelocity impacted films. Due to this effect, an impacted pure polyimide film (0 wt.% POSS) eroded one order of magnitude faster than impacted 15 wt.% POSS-containing film. The accelerated erosion of the 0 wt.% POSS sample is characterized mainly by the formation of AO-induced new holes. These holes tend to be formed in a radial star-like pattern around the sample's central impact zone. A model explaining this phenomenon is suggested based on residual tensile stresses, which are also established in a star-like pattern, as a result of the ultrahigh-velocity impact. These residual stresses generate a local increase in the polymer free volume, which facilitates oxygen diffusion into the bulk of the polymer, thus initiating the process of local high-rate degradation. Due to this mechanism, the AO-induced new holes replicate the star-like pattern. The low erosion rate of the impacted 15 wt.% POSS-containing film is therefore attributed to both mechanical (i.e. negligible residual tensile stresses) and chemical (i.e. formation of an oxide passivation layer) mechanisms.

Acknowledgements: This work was supported in part by the Israeli Space Agency. The authors are grateful to J. Lichtenhan from Hybrid Plastics and A. Laikhtman and G. Lempert from Soreq NRC for useful discussions. The authors are also grateful to M. Freankel, S. Maman, S. David and D. Shkolnik (Soreq NRC) for their technical support.

NOTE

1. Author to whom correspondence should be addressed: e-mail: rverker@soreq.gov.il

REFERENCES

[1] Grossman, E., Gouzman, I., Viel-Inguimbert, I. and Diguirard, M. (2003). Modification of a 5-eV atomic-oxygen laser detonation source. *J. Spacecraft and Rockets,* **40**: 110.

[2] Houdayer, A., Cerny, G., Klemberg-Sapieha, J. E., Czeremuszkin, G. and Wertheimer, M. R. (1997). MeV proton irradiations and atomic oxygen exposure of spacecraft materials with SiO2 protective coatings. *Nucl. Instrum. Methods Phys. Res. B,* **131**: 335.

[3] Tennyson, R. C. and Shortliffe, G., (1997). MOD impact damage on composite materials in space In *Proc. 7th Inter. Symp. Mater. in Space Env.* ESA Publication, ESTEC Noordwijk, The Netherlands.

[4] Hastings, D. and Garrett, H. (1996). *Spacecraft-Environment Interactions*. Cambridge University Press, Cambridge, UK, p.45.

[5] Miao, J. and Stark, J. P. W. (2001). Direct simulation of meteoroids and space debris flux on LDEF spacecraft surfaces. *Planetary and Space Sci.*, **49**: 927.

[6] Silverman, E. M. (1995). *Space Environmental Effects on Spacecraft – LEO Material Selection Guide*, *NASA Contractor Report No. 4661*. Langley Research Center, p. 1–4.

[7] Stein, C., Roybal, R. and Tlomak, P. (2000). The production of contamination on spacecraft surfaces by hypervelocity debris impacts. In *Proc. 8th Inter. Symp. Mater. in Space Env.* CNES Publication, Toulouse, France.

[8] Medina, D. F., Wright, L. and Campbell, M. (2001). Parametric investigation of solar panel hypervelocity impact damage. *Adv. Space Res.,* **28**: 1347.

[9] Rutledgs, S. K. and Olle, R. M. (1993). Space station freedom solar array blanket coverlay atomic oxygen durability testing results. In *Proc. 38th Inter. Symp. SAMPE Symposium.* Anheim, California, USA.

[10] Brunsvold, A. L., Minton, T. K., Gouzman, I., Grossman, E. and Gonzales, R. (2004). An investigation of the resistance of polyhedral oligomeric silsesquioxane polyimide to atomic-oxygen attack. *High Performance Polymers,* **16**: 303.

[11] Gilman, J. W., Schlitzer, D. S. and Lichtenhan, J. D. (1996). Low earth orbit resistant siloxane copolymers. *J. Applied Polymer Sience,* **60**: 591.

[12] Gonzales, R. I. (2002). Synthesis and In-Situ Atomic Oxygen Erosion Studies of Space Survivable Hybrid Organic/Inorganic Polyhedral Oligomeric Silsesquioxane Polymers. Ph.D. Thesis, University of Florida, USA.

[13] Philips, S. H., Haddad, T. S. and Tomczak, S. J. (2004). Developments in nanoscience: polyhedral oligomeric silsesquioxane (POSS)-polymers. *Current Opinion in Solid State and Materials Science,* **8**: 21.

[14] Lichtenhan, J. (2006). Private Communication.

[15] Fu, B. X. (2005). Private Communication.

[16] Tighe, A., Gabriel, S. and Van Eesbeek, M. (2000). Ground based simulation of orbital debris using laser driven flyer plates. In *Proc. 8th Inter. Symp. Mater in Space Env.* CNES Publication, Toulouse, France.

[17] Roybal, R., Tlomak, P., Stein, C. and Stokes, H. (1999). Simulated space debris impact experiments on toughened laminated thin solar cell cover glass. *Inter. J. Impact Eng.*, **23**: 811.

[18] Eliezer, S. (2002). The Interaction of High-Power Lasers with Plasmas. Institute of Physics, Bristol, UK.

[19] Gouzman, I., Grossman, E., Lempert, G., Noter, Y., Lifshitz, Y., Viel-Inguimbert, V. and Dinguirard, M. (2004). Atomic-oxygen durability of a silicone paint: comparison between two simulation methods. *J. Spacecraft and Rockets,* **41**: 350.

[20] Intrater, R., Lempert, G., Gouzman, I., Grossman, E., Cohen, Y., Rein, D. M., Khakfin, R. L. and Hoffman, A. (2004). Simulated low Earth orbit environment interaction with different types of polyethylene. *High Performance Polymers,* **16**: 249.

[21] ASTM E-2089-00. (2002). Standard practices for ground laboratory atomic oxygen interaction evaluation of materials for space applications. In: Annual book of ASTM standards, vol. 15.03. West Conshohocken, PA, USA: ASTM International, p. 752.

[22] Hybrid Plastics, Inc., Technical bulletin, http://www.hybridplastics.com/pdf/POSS-Kapton%20PI%20 Spec.pdf.

[23] Du-Pont. Inc. (1993). Technical Bulletin, PYRALIN® Polyimide Coating PI 2545 PI 2540 Product Information.

[24] Verker, R., Eliaz, N., Gouzman, I., Eliezer, S., Fraenkel, M., Maman, S., Beckmann, F., Pranzas, K. and Grossman, E. (2004). The effect of simulated hypervelocity space debris on polymers. *Acta Materialia,* **52**: 5539.

[25] Verker, R., Grossman, E., Gouzman, I., Laikhtman, A., Katz, S., Freankel, M., Maman, S., Lempert, G. and Eliaz, N. (2006). Mechanical and morphological behavior of POSS-polyimide films under hypervelocity impacts and atomic oxygen exposure. *Soreq NRC Report No. 3689.*

[26] Verker, R., Grossman, E., Gouzman, I. and Eliaz, N. (2007). Residual Stress Effect on Degradation of Polyimide under Simulated Hypervelocity Space Debris and Atomic Oxygen. *Polymer*, **48**: 19.

[27] Klopffer, M. H. and Flaconnèche, B. (2001). Transport properties of gases in polymers: bibliographic review. *Oil & Gas Science and Technology – Rev. IFP*, **56**: 223.

[28] Larche, F. C. and Cahn, W. J. (1982). The Effect of Self-Stress on Diffusion in Solids. *Acta Metall*., **30**: 1835.

[29] Oriani, R. A. (1969). Hydrogen in metals. In *Proc. of the conference on fundamental aspects of stress corrosion cracking*, National Association of Corrosion Engineers, Houston, Texas.

[30] Eliaz, N. and Banks-Sills, L. (2008). Chemical potential, diffusion and stress – common confusions in nomenclature and units. *Corrosion Reviews*, **26(2–3)**: 87–103.

[31] Tyler, D. R. (2004). Mechanistic aspects of the effects of stress on the rates of photochemical degradation reactions in polymers. *Journal of Macromolecular Science,* **44**: 351.

[32] O'Donnell, J. B. and White, J. R. (1994). Photo-oxidation of polystyrene under load. *Journal of Materials Science,* **29**: 3955.

[33] Whitaker, A. F. and Jang, B. Z. (1993). The mass loss mechanism of polymers in a radio frequency induced atomic oxygen environment. *Journal of Applied Polymer Science,* **48:** 1341.

[34] Klein, R. and Scheer, M. D. (1968). Mechanism of O(3P) Addition to Condensed Films. II. Propene, 1-Butene, and Their Mixtures. *The Journal of Physical Chemistry*, **72**: 616.

[35] Grossman, E., Gouzman, I., Lempert, G., Noter, Y. and Lifshitz, Y. (2004). Assessment of Atomic Oxygen flux in LEO ground simulation facilities. *Journal of Spacecraft and Rockets* **41**: 356.